A&A 519, A4 (2010)
DOI: 10.1051/0004-6361/200912001

Astronomy & Astrophysics

Reconstruction of the cosmic microwave background lensing for *Planck*

L. Perotto[1,2], J. Bobin[3,4], S. Plaszczynski[2], J.-L. Starck[3], and A. Lavabre[2]

[1] Laboratoire de Physique Subatomique et de Cosmologie (LPSC), CNRS: UMR5821, IN2P3, Université Joseph Fourier – Grenoble I, Institut Polytechnique de Grenoble, France
e-mail: perotto@lpsc.in2p3.fr
[2] Laboratoire de l'Accélérateur Linéaire (LAL), CNRS: UMR8607, IN2P3, Université Paris-Sud, Orsay, France
e-mail: plaszczy@lal.in2p3.fr,lavabre@lal.in2p3.fr
[3] Laboratoire AIM (UMR 7158), CEA/DSM-CNRS-Université Paris Diderot, IRFU, SEDI-SAP, Service d'Astrophysique, Centre de Saclay, 91191 Gif-Sur-Yvette Cedex, France
e-mail: jstarck@cea.fr
[4] Applied and Computational Mathematics (ACM), California Institute of Technology, 1200 E.California Bvd, M/C 217-50, PASADENA CA-91125, USA
e-mail: bobin@acm.caltech.edu

Received 6 March 2009 / Accepted 19 February 2010

ABSTRACT

Aims. We prepare real-life cosmic microwave background (CMB) lensing extraction with the forthcoming *Planck* satellite data by studying two systematic effects related to the foreground contamination: the impact of foreground residuals after a component separation on the lensed CMB map, and the impact of removing a large contaminated region of the sky.
Methods. We first use the generalized morphological component analysis (GMCA) method to perform a component separation within a simplified framework, which allows a high statistics Monte-Carlo study. For the second systematic, we apply a realistic mask on the temperature maps and then restore them with a recently developed inpainting technique on the sphere. We investigate the reconstruction of the CMB lensing from the resultant maps using a quadratic estimator in the flat sky limit and on the full sphere.
Results. We find that the foreground residuals from the GMCA method does not significantly alter the lensed signal, which is also true for the mask corrected with the inpainting method, even in the presence of point source residuals.

Key words. cosmic microwave background – large-scale structure of Universe – gravitational lensing: weak – methods: statistical

1. Introduction

Cosmic microwave background (CMB) temperature anisotropies and polarization measurements have been one of the key cosmological probes to establish the current cosmological constant Λ and cold dark matter (ΛCDM) paradigm. Reaching the most precise measurement of these observables is the main scientific goal of the forthcoming or ongoing CMB experiments – like the European Spacial Agency satellite *Planck*[1], which was successfully launched on the 14th of May 2009 and has currently begun collecting data.

Planck is designed to deliver full-sky coverage, low-level noise, high resolution temperature and polarization maps (see Tauber 2006; The *Planck* Consortia 2005). With these high quality observations it will be possible to extract cosmological informations from the CMB maps beyond the angular power spectra (two-points correlations, hereafter APS), by exploiting the measurable non-Gaussianities (see e.g. Komatsu 2002; The *Planck* Consortia 2005).

The weak gravitational lensing is one of the sources of non-Gaussianity affecting the CMB after the recombination (see Lewis & Challinor 2006 for a review). The CMB photons are weakly deflected by the gravitational potential of the intervening large-scale structures (LSS), which perturb the Gaussian statistic of the CMB anisotropies (Bernardeau 1997; Zaldarriaga 2000). Conversely, it becomes possible to reconstruct the underlying gravitational potential by exploiting the higher-order correlations induced by the weak lensing in the CMB maps (Bernardeau 1997; Guzik et al. 2000; Takada & Futamase 2001; Hu 2001b; Hirata & Seljak 2003a).

The relevance of the CMB lensing reconstruction for the cosmology is twofold. First, for the sake of measuring the primordial B-mode of polarization predicted by the inflationary models (Kamionkowski et al. 1997; Seljak & Zaldarriaga 1997), the CMB lensing is a major contaminant. It induces a secondary B-mode polarization signal in perturbing the E-mode polarization pattern (Zaldarriaga & Seljak 1998). A lensing reconstruction allowing the *delensing* of the CMB maps is required to recover the primordial B-mode signal (Knox & Song 2002; Seljak & Hirata 2004). However, CMB lensing is also a powerful cosmological probe of the matter distribution integrated from the last scattering surface to us. This will soon be a unique opportunity to probe the full-sky LSS distribution, with a maximum efficiency at redshift around 3, where structures still experience a well described linear growth (Lewis & Challinor 2006). A lensing reconstruction would largely improve the sensitivity of the CMB experiments to the cosmological parameters that affect the growth of

[1] http://www.rssd.esa.int/index.php?project=PLANCK\&page=index

the LSS, like neutrino mass or dark energy (Hu 2002; Kaplinghat et al. 2003; Lesgourgues et al. 2006; Perotto et al. 2006).

Although well-known theoretically (Blanchard & Schneider 1987), the CMB lensing has never been directly measured. Smith et al. (2007) and Hirata et al. (2008) have found evidence for a detection of the CMB lensing in the WMAP data by correlating them with several other LSS probes (Luminous Red Galaxies, Quasars and radio sources) at 3.4σ and 2.5σ level respectively. This situation is expected to change with the forthcoming *Planck* data. *Planck* will be the first CMB experiment allowing the measurement of the underlying gravitational potential without requiring any external data. However, even with the never before met quality of the *Planck* data, CMB lensing reconstruction will be challenging. The lensing of the CMB is a very subtle secondary effect, affecting the smaller angular scale at the limit of the *Planck* resolution in a correlated way over several degrees on the sky. As already quoted, its reconstruction is based on the induced non-Gaussianities in the CMB maps in the form of mode coupling. Consequently, any process resulting in coupling different Fourier moments is a challenging systematic to deal with in order to retrieve the lensing signal (see Su & Yadav 2009 for a recent study of the impact of instrumental systematics on the CMB lensing reconstruction bias). Astrophysical components and other secondary effects could also be a source of non-Gaussianity. These components include thermal and kinetic Sunyaev-Zel'dovich effects (thSZ and kSZ), due to the scattering of CMB radiation by electrons within the galaxy clusters (Sunyaev & Zeldovich 1970); foreground emissions like synchrotron, Bremsstrahlung and dust-diffuse galactic emission as well as extragalactic point sources. All these components may give a sizable contribution to the level of non-Gaussianities in the CMB maps (Aghanim & Forni 1999; Argüeso et al. 2003; Amblard et al. 2004; Riquelme & Spergel 2007; Babich & Pierpaoli 2008).

The impact of most of the aforementioned effects on the CMB lensing analysis with WMAP data has been investigated by Hirata et al. (2008). They found a negligible contamination level, which is encouraging. However, such a result could change when one considers the higher resolution, better sensitivity maps provided by *Planck*. In Barreiro et al. (2006) the component separation impact on non-Gaussianity was studied in the framework of the *Planck* project, but no lensing reconstruction was performed. Hence the impact of these foreground residuals on the CMB lensing reconstruction is still to be studied.

The overall purpose of the present study is to give an insight to the issues we should deal with before undertaking any complete study of the CMB lensing retrieval with *Planck*: what is the impact of the foreground residuals on the CMB lensing reconstruction? Will it still be possible to reconstruct the CMB lensing after a component separation process, or will such a process alter the temperature map statistics? How should we deal with the masking issue? Beyond the *detection* of the CMB lensing signal, we tackled the *reconstruction* of the underlying projected potential APS. We investigated two issues, the impact of a component separation algorithm on the lensing reconstruction and the impact of a masked temperature map restoration before applying a deflection estimator.

Section 2 briefly reviews the CMB lensing effect and the reconstruction method. We present in Sect. 3 an analysis of the impact of one component separation technique, named *generalized morphological component Analysis* (GMCA) (Bobin et al. 2008), which is one of the different methods investigated by the *Planck* consortium (Leach et al. 2008). In Sect. 4, we show how a recently developed gap-filling method (i.e. inpainting process) (Abrial et al. 2008) may solve the masking problem, which may be one of the major issues for the CMB lensing retrieval because it introduces some misleading correlations between different angular scales in the maps.

2. CMB lensing

In this section, we briefly review the CMB lensing effect and the reconstruction method. We introduce the notations used throughout this paper.

The geodesic of the CMB photons is weakly deflected by the gravitational potential from the last scattering surface to us. Observationally this effect results in a remapping of the CMB temperature anisotropies $T = \Delta\Theta/\Theta_{\rm CMB}$, according to Blanchard & Schneider (1987):

$$\widetilde{T}(\hat{\boldsymbol{n}}) = T(\hat{\boldsymbol{n}} + \boldsymbol{d}(\hat{\boldsymbol{n}})). \tag{1}$$

In words, the lensed temperature $\widetilde{T}$ in a given direction of the sky $\hat{\boldsymbol{n}}$ is the temperature T one would have seen in the neighboring direction $\hat{\boldsymbol{n}} + \boldsymbol{d}(\hat{\boldsymbol{n}})$ in the absence of any intervening mass. The deflection angle, $\boldsymbol{d}(\hat{\boldsymbol{n}})$, is the gradient of the line-of-sight projection of the gravitational potential[2], $\boldsymbol{d}(\hat{\boldsymbol{n}}) = \boldsymbol{\nabla}\phi(\hat{\boldsymbol{n}})$, where ϕ can be calculated within the Born approximation as the integral along the line-of-sight of the tridimensional gravitational potential (Challinor & Lewis 2005).

The CMB lensing probes the intervening mass in a broad range of redshifts, from $z_* = 1090$ at the last scattering surface to $z = 0$, with a maximum efficiency at $z \sim 3$. At this high redshift, the LSS responsible for the CMB lensing (with a typical scale of 300 h^{-1} Mpc) still experience a linear regime of growth. As a result the projected potential ϕ can be assumed to be a Gaussian random field. The consequences of the nonlinear corrections to ϕ are shown to be weak on the CMB lensed observables (Challinor & Lewis 2005). Thus, this hypothesis holds very well as long as the CMB lensing study does not aim at measuring a correlation with other LSS probes at lower redshifts.

Besides, the deflection angles have a rms of $\simeq$2.7 arcmin in the standard ΛCDM model and can be correlated over several degrees on the sky. The typical scales of the lensing effects are small enough for a convenient analysis within the flat-sky approximation. The projected potential may be decomposed on a Fourier basis $\phi(\boldsymbol{k})$, and its statistics is completely defined by

$$\langle\phi(\boldsymbol{k}_1)\phi(\boldsymbol{k}_2)\rangle = (2\pi)^2\delta(\boldsymbol{k}_1 + \boldsymbol{k}_2)\, C^{\phi\phi}_{k_1}, \tag{2}$$

where $C^{\phi\phi}_{k_1}$ is the full-sky projected potential APS taken at a multipole $l = |\boldsymbol{k}_1|$ and is related to the deflection APS by

$$C^{\rm dd}_k = k^2 C^{\phi\phi}_k. \tag{3}$$

The lensed CMB temperature APS can be derived from the Fourier transform of Eq. (1) (e.g. as in Okamoto & Hu 2003). The lensing effect slightly modifies the APS of the CMB temperature, weakly smoothing the power at all angular scale to the benefit of the smaller angular scales. Deeply in the damping tail, at multipole $l \gtrsim 3000$ lensing contribution even dominates over the pure CMB one. However, the main observational consequences of the CMB lensing effect lie beyond the APS. The

[2] A priori, the remapping function should depend not only on a convergence field but also on a rotation field, so that the deflection angle is not purely gradient but has a rotational contribution. However, Hirata & Seljak (2003b) have shown that the rotation field effect will be negligible for the next generation of CMB experiments.

remapping induces non-Gaussianities in the CMB temperature field in the form of some correlations between different angular scales.

Consequently, the two-point correlation function of the lensed temperature modes, calculated at the first order in ϕ, is written as (Okamoto & Hu 2003)

$$\begin{aligned}\langle\widetilde{T}(\boldsymbol{k}_1)\widetilde{T}(\boldsymbol{k}_2)\rangle_{\rm CMB} &= (2\pi)^2\delta(\boldsymbol{k}_1+\boldsymbol{k}_2)\,\widetilde{C}^{\rm TT}_{k_1} \\ &+ f_{\rm TT}(\boldsymbol{k}_1,\boldsymbol{k}_2)\,\phi(\boldsymbol{L})+O(\phi^2),\end{aligned} \tag{4}$$

where $\boldsymbol{L}=\boldsymbol{k}_1+\boldsymbol{k}_2$, and the CMB subscript denotes an ensemble average over different realizations of the CMB, but over a fixed integrated potential field. The weighting function $f_{\rm TT}$ depends on the primordial temperature APS like this

$$f_{\rm TT}(\boldsymbol{k}_1,\boldsymbol{k}_2)=\boldsymbol{L}\cdot\boldsymbol{k}_1\,C^{\rm TT}_{k_1}+\boldsymbol{L}\cdot\boldsymbol{k}_2\,C^{\rm TT}_{k_2}. \tag{5}$$

Similarly, one can calculate the four-point correlation function of the CMB temperature field – as in Kesden et al. (2003). One finds that the trispectrum of the lensed temperature field – or equivalently, the connected part of its four-point correlation function – is non-null even if the underlying (unlensed) temperature field is purely Gaussian.

Two possible ways were developed to deal with the reconstruction of the integrated gravitational potential field from a lensed CMB map. One was described by Hirata & Seljak (2003a,b), whose maximum-likelihood estimator method aims to increase the capabilities of the highest sensitivity highest resolution CMB projects in reconstructing the integrated potential. The other was developed by Hu (2001b); Hu & Okamoto (2002); Okamoto & Hu (2003), whose quadratic estimator approach is still close to optimal for currently built experiments like *Planck*. Accordingly we adopt this method throughout this work.

In the flat sky approximation, the estimated potential map takes the following form (Okamoto & Hu 2003):

$$\widehat{\phi}_{\rm TT}(\boldsymbol{L})=\frac{A_{\rm TT}(L)}{L^2}\int\frac{{\rm d}^2\boldsymbol{k}_1}{(2\pi)^2}\,\bar{T}(\boldsymbol{k}_1)\bar{T}(\boldsymbol{k}_2)F_{\rm TT}(\boldsymbol{k}_1,\boldsymbol{k}_2)\,, \tag{6}$$

where the Fourier modes $\bar{T}(\boldsymbol{k})$ refer to the *observed* temperature modes, affected by both the CMB lensing and the instrumental noise of the CMB experiment concerned. More precisely, the temperature map is assumed to be contaminated by an additional white Gaussian noise and deconvolved from a beam function assumed to be Gaussian, so that its APS reads

$$\langle\bar{T}(\boldsymbol{k}_1)\bar{T}(\boldsymbol{k}_2)\rangle=(2\pi)^2\,\delta(\boldsymbol{k}_1+\boldsymbol{k}_2)\left(\widetilde{C}^{\rm TT}_{k_1}+N^{\rm TT}_{k_1}\right), \tag{7}$$

where $N^{\rm TT}_{k_1}$ is the instrumental noise APS, modeled in this analysis as

$$N^{\rm TT}_{k}=\theta^2_{\rm fwhm}\sigma^2_{\rm T}\,\exp\left[k^2\frac{\theta^2_{\rm fwhm}}{8\ln 2}\right], \tag{8}$$

where $\theta_{\rm fwhm}$ is the full-width at half maximum (FWHM) of the beam function and $\sigma_{\rm T}$, the root mean square of the noise per resolution elements.

Besides, the normalization function is calculated so that $\widehat{\phi}_{\rm TT}(\boldsymbol{L})$ is an unbiased estimator of the integrated potential field

$$A_{\rm TT}(L)=L^2\left[\int\frac{{\rm d}^2\boldsymbol{k}_1}{(2\pi)^2}\,f_{\rm TT}(\boldsymbol{k}_1,\boldsymbol{k}_2)F_{\rm TT}(\boldsymbol{k}_1,\boldsymbol{k}_2)\right]^{-1}. \tag{9}$$

Then the weighting function $F_{\rm TT}$ is adjusted to minimize the dominant contribution to the estimator variance, i. e. the unconnected part of the quantity $\langle\hat{\phi}_{\rm TT}(\boldsymbol{L})\hat{\phi}_{\rm TT}(\boldsymbol{L}')\rangle-(2\pi)^2\,\delta(\boldsymbol{L}+\boldsymbol{L}')C^{\phi\phi}_L$. Derived in Okamoto & Hu (2003), the calculation leads to

$$F_{\rm TT}(\boldsymbol{k}_1,\boldsymbol{k}_2)=\frac{f_{\rm TT}(\boldsymbol{k}_1,\boldsymbol{k}_2)}{2\bar{C}^{\rm TT}_{k_1}\bar{C}^{\rm TT}_{k_2}}, \tag{10}$$

where $\bar{C}^{\rm TT}_k\equiv\widetilde{C}^{\rm TT}_k+N^{\rm TT}_k$ is the *observed* temperature power APS as defined in Eq. (7).

Finally, the covariance of the integrated potential field estimator provides us with a four-point estimator of the integrated potential APS. When expanding the lensed CMB temperature modes at second order in ϕ, the $\widehat{\phi}_{\rm TT}$ estimator covariance reads

$$\langle\hat{\phi}_{\rm TT}(\boldsymbol{L})\hat{\phi}_{\rm TT}(\boldsymbol{L}')\rangle=(2\pi)^2\,\delta(\boldsymbol{L}+\boldsymbol{L}')\,C^{\phi\phi}_{\rm TT,TT}(L)\,, \tag{11}$$

where the estimated potential APS, $C^{\phi\phi}_{\rm TT,TT}(L)$, taking into account all sources of variances, both projected potential and CMB cosmic variance, instrumental noise and confusion noise from other potential Fourier modes, writes

$$C^{\phi\phi}_{\rm TT,TT}(L)=C^{\phi\phi}_L+N^{\phi\phi}_{(0)}(L)+N^{\phi\phi}_{(1)}(L)+N^{\phi\phi}_{(2)}(L). \tag{12}$$

Here we have distinguished three different noise contributions to the integrated potential estimator variance. The dominant noise contribution, $N^{\phi\phi}_{(0)}(L)=A_{\rm TT}(L)$, depends only on the unlensed and the observed temperature APS. It represents the Gaussian contribution to the potential APS estimator, in the sense that it is the variance one would obtain by replacing the lensed temperature map in Eq. (6) by a map with the same APS but Gaussian statistics. In addition, the potential APS estimator suffers from sub-dominant non-Gaussian noise contributions. The first, quoted $N^{\phi\phi}_{(1)}(L)$, was calculated by Kesden et al. (2003). The second non-Gaussian noise term $N^{\phi\phi}_{(2)}(L)$ is quadratic in $C^{\phi\phi}_L$. First calculated in Hanson et al. (2010), this term is shown to contribute even more than the first-order one at low multipoles ($L\leq 200$).

These two non-Gaussian noise terms arise from the trispectrum part (or so-called connected part) of the four-point lensed temperature correlator hidden in the integrated potential field estimator covariance. It can be interpreted as the confusion noise coming from other integrated potential modes. Because it depends on the integrated potential APS, which has to be estimated, an iterative estimation scheme would be required for taking it into account. However, our study based on simulated data allows us to calculate these terms from the fiducial potential APS and then subtract it from the estimator variance.

3. Effect of foreground removal: a Monte-Carlo analysis

Up to now, no analysis has been performed to assess the effect of a component separation process on the CMB lensing extraction. The question we propose to address here is whether the lensing signal is preserved in the CMB map output by the component separation process. In order to get a first insight, we use a Monte-Carlo approach within the flat sky approximation.

3.1. Idealized Planck sky model

We created a simulation pipeline to generate some idealized synthetic patches of the sky for the *Planck* experiment. Our

sky model is a linear uncorrelated mixture of the lensed CMB temperature and astrophysical components, which includes the Sunyaev-Zel'dovich effect, the thermal emission of the interstellar dust and the unresolved infrared point sources emission. In modeling these three components, we made sure to catch the dominant foreground emission features at the *Planck*-HFI frequencies. Then we added the nominal effects of the *Planck*-HFI instrument, modeled as a purely Gaussian-shaped beam and a spatially uniform white Gaussian noise. Each hypothesis we adopted is a crude model of the astrophysical contaminant and systematic effects that pollute the *Planck* data, and is intended to be a *demonstration model* for a study devoted to the impact of the component separation algorithms on the CMB lensing retrieval.

We generated four sets of 300 *Planck*-HFI synthetic patches of the sky, with instrumental noise and, when needed, with foreground emissions.

- Set I contains lensed CMB temperature maps generated from an unique fixed projected potential realization and with the instrumental effects (beam and white noise);
- Set I-fg is built from Set I. In addition, a fixed realization of dust and SZ was added to each Set I map;
- Set II is a set of lensed CMB temperature maps generated from 300 random realizations of the lenses distribution plus the instrumental effects;
- Set II-fg is built from Set II. Each map of Set II is superimposed with one of each foreground maps out of the available 30 dust maps, located at high galactic latitude ($|\theta| < 30°$), and 1500 SZ maps.

Note that the point sources emission will be included afterward in our simulation pipeline through a direct estimation of the point source residuals after component separation as described in Sect. 3.2. Sets I and I-fg will serve to study the projected potential *field* reconstruction, whereas Sets II and II-fg will be used in the projected potential *angular power spectrum* (APS) estimate analysis. Our method and its assumed hypothesis are detailed below.

3.1.1. Lensed CMB temperature map

Once we assumed the Gaussianity of the integrated potential field, the lensed CMB temperature simulation principle is straightforward as a direct application of the remapping Eq. (1). We started from the APS of both the temperature and the projected potential field as well as the cross-APS reflecting the correlation between the CMB temperature and the gravitational potential fields due to the Integrated Sachs-Wolfe (ISW) effect. Then we generated two Gaussian fields directly in the Fourier space, so that

$$T(\boldsymbol{k}) = \sqrt{C^{\rm TT}_{|\boldsymbol{k}|}}\, G^{(1)}_{(0,1)}(\boldsymbol{k}) \tag{13}$$

$$\phi(\boldsymbol{k}) = \sqrt{\frac{(C^{{\rm T}\phi}_{|\boldsymbol{k}|})^2}{C^{\rm TT}_{|\boldsymbol{k}|}}}\, G^{(1)}_{(0,1)}(\boldsymbol{k}) + \sqrt{C^{\phi\phi}_{|\boldsymbol{k}|} - \frac{(C^{{\rm T}\phi}_{|\boldsymbol{k}|})^2}{C^{\rm TT}_{|\boldsymbol{k}|}}}\, G^{(2)}_{(0,1)}(\boldsymbol{k}),$$

where $G^{(1)}_{(0,1)}(\boldsymbol{k})$ and $G^{(2)}_{(0,1)}(\boldsymbol{k})$ are two independent realizations of a Gaussian field of zero mean and unit variance. Because of the typical scales of the deflection field – deflection angles are of the order of 2 or 3 arcmin (depending on the fiducial cosmological model) but correlated over several degrees on the sky – the generated maps should be both high resolution and extended over a large sky area. We choose to produce some 12.5×12.5 square degrees maps of 2.5 arcmin of resolution, as a good trade-off between the quality of the simulated maps and the time needed to the generation and the analysis of these maps.

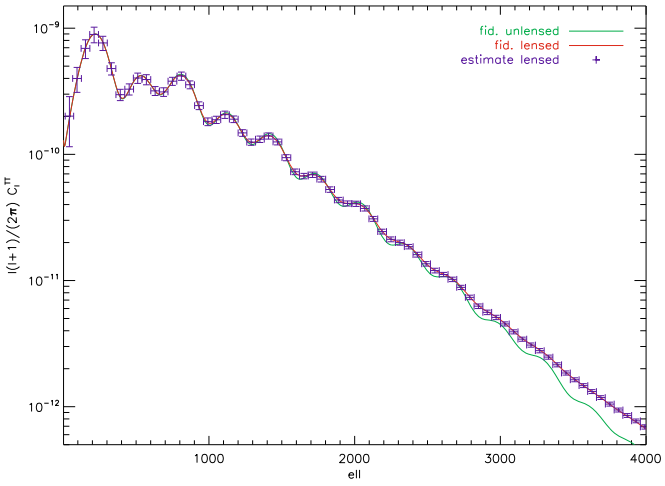

Fig. 1. CMB temperature APS. The red/black (respectively green/grey) line is the lensed (respectively unlensed) temperature APS calculated with the public Boltzmann code CAMB (Lewis et al. 2000; Challinor & Lewis 2005). The blue/black data-points are the mean of the binned power spectrum reconstructed on 500 simulated lensed temperature maps. The error-bars are given by the variance of the 500 APS estimates.

From CMB temperature and projected potential in the Fourier space, we calculated both the temperature and the deflection angles in the real space. The last step consisted in performing the remapping of the primordial temperature map according to the deflection angles. Here is the technical point. Starting from a regular sample of a field (the underlying unlensed map), we have to extract an irregular sample of the same field (the lensed map) – the new directions where to sample from are given by the previous one shifted by the deflection angles. Thus, this is a well-documented interpolation issue, the difficulty lying in the fact that the scale of the interpolation scheme is the same as the typical scale of the physical process of interest. We took particular care in the interpolation algorithm to avoid creating some spurious lensing signal or introducing additional non-Gaussianities. We found that a parametric cubic interpolation scheme (Park & Schowengerdt 1983) fitted reasonably well. In addition, to avoid any loss of power due to the interpolation, we overpixellized twice the underlying unlensed temperature and deflection field. The first test we performed to control the quality of the simulation was to compare the Monte-Carlo estimate of the APS over 500 simulations of the lensed maps to the analytical calculation of the lensed APS provided by the CAMB[3] Boltzmann code (Lewis et al. 2000; Challinor & Lewis 2005). As shown in Fig. 1, the APS of our simulated lensed maps is consistent with the theoretical one up to multipole 4000 – which is large enough to study the CMB lensing with *Planck*.

3.1.2. Astrophysical components

In any CMB experiment the temperature signal is mixed with foreground contributions of astrophysical origin – among them we can separate the diffuse galactic emission (thermal and rotational dust, synchrotron, Bremsstrahlung (free-free) radiation)

[3] Web site: http://camb.info/

Table 1. Instrumental characteristics of *Planck*-HFI[a].

channel (GHz)	$\theta_{\rm fwhm}$ (arcmin)	$\sigma_{\rm T}$ (μK.sr$^{-0.5}$)
100	9.5	6.8
143	7.1	6.0
217	5.	13.1
353	5.	40.1
545	5.	401
857	5.	18 300.

Notes. [(a)] (See The *Planck* Consortia 2005).

from the extragalactic components (point sources, thermal and kinetic Sunyaev-Zel'dovich effects). As discussed in the introduction, each of these components could potentially, if inefficiently removed, degrade our capability to reconstruct the CMB lensing. Here, to complete our demonstration sky model, we choose to simulate the dominant astrophysical foregrounds at the *Planck*-HFI frequencies, namely the thermal emission of the galactic dust, the thermal SZ effect and the unresolved infrared point sources. Thermal dust templates are obtained from the 100 μm IRAS data in the sky region located around $\alpha = 204°$ and $\delta = 11°$, as described in Delabrouille et al. (2003). Note that several treatments were applied on these maps – point sources removal, destriping, inpainting in the Fourier space with constraint realizations – which may induce an amount of additional non-Gaussianities. We selected 30 IRAS dust templates whose root mean square temperatures lie in the range .6 to 6.75 microkelvins Rayleigh-Jeans. The SZ emission on the sky patches can be randomly selected in a set of 1500 realizations produced with a semi-analytical simulation tool provided in the literature (Delabrouille et al. 2002). Note that the SZ emission is assumed here not to correlate with the CMB lensed signal. As for the estimates of the unresolved point source residuals, we choose to take advantage of the refined full-sky simulations of the infra-red point sources emission in each *Planck*-HFI frequencies provided by the *Planck component separation working group* (WG2). In these simulations, the source counts are drawn from the IRAS catalog, and their spectral energy distributions are modeled following Serjeant & Harrison (2005). In addition, they involve several refinements like the filling of the IRAS mask by synthetic data, the additional simulation of fainter sources according to the Granato et al. (2004) model, and their clustering (see Leach et al. 2008). Note that the radio-galaxies, another population of extragalactic sources, can be safely neglected here, as they lead to a sub-dominant emission compared to that of the infrared-galaxies at the *Planck*-HFI frequencies.

3.1.3. *Planck*-like noise

Finally, we simulated the effects of the *Planck* High Frequency Instrument (HFI) according to their nominal characteristics (The *Planck* Consortia 2005), which are summarized in Table 1. At each frequency channel, the component mixture was convolved with a Gaussian beam with the corresponding FWHM size. Then a spatially uniform white noise following a Gaussian statistic was added. Finally, the resulting maps were deconvolved from the beam transfer function, resulting in an exponential increase of the noise at the scales corresponding to the beam size. Because smaller angular scales carry the larger amount of lensing information, the higher the angular resolution is, the better the lensing reconstruction can be. Our tests show that in the ideal case the lensing reconstruction on *Planck*-HFI synthetic maps is insensitive to the addition or the removal of the 100 GHz frequency channel information, whose beam function is roughly twice as large as the beam in the higher frequency channels. It was even worse when we ran the full Monte-Carlo chain, because after turning the foreground emission and component separation process on, the addition of the lower frequency channel resulted in increasing the confusion noise of the lensing reconstruction. That was the reason we excluded the 100 GHz frequency channel from our analysis. To summarize, our *Planck* sky model reads

$$\mathsf{T}^{\rm obs} = \mathcal{A}\,\mathsf{s} + \mathsf{B}^{-1} \otimes \mathsf{n}, \tag{14}$$

where $\mathsf{T}^{\rm obs}$ is the set of five individual frequency channel maps, $\mathcal{A}$ is the mixing matrix calculated from the frequency dependence of the three signal contributions, s is the set of CMB, dust and SZ maps at a pivot frequency, B^{-1} is the set of Gaussian beam inverse transfer functions and n the set of white noise maps in the five frequency channels we selected. Note that we assumed a perfect beam-deconvolution process.

3.2. Component separation using the generalized morphological component analysis

For most of the cosmological analysis of the CMB data – and for the CMB lensing extraction in particular – the cosmological signal has to be carefully disentangled from the other sources of emission that contribute to the observed temperature map. The component separation is a part of the signal processing dedicated to distinguish between the different contributions of the final maps. Briefly, the gist of any component separation technique consists in taking advantage of the difference in the frequency behavior and the spatial structures (i.e. morphology) that distinguish these different *components*. From a set of frequency channel maps, a typical component separation algorithm provides a unique map of the CMB temperature with the instrumental noise and a foreground emission residual. In general, the lower the foreground residual rms level, the better the separation algorithm. However, this simple rule is not necessarily true for CMB lensing reconstruction. In this case, preserving the statistical properties of the underlying CMB temperature map is critical.

In the *Planck* consortium, the component separation is a critical issue, involving a whole working group (WG2) devoted to provide several algorithms for separating CMB from foregrounds and to compare their merits (see Leach et al. 2008 for a recent comparison of the current proposed methods). Eight teams have provided a complete component separation pipeline capable to treat a realistic set of *Planck* temperature and polarization maps. Each method differs in the external constraints they use, the physical modeling they assume and the algorithm they are based on.

Among the available techniques we choose to use the generalized morphological component analysis (hereafter GMCA), which is a blind component separation method. In the GMCA, each observation $T_\nu^{\rm obs}(\hat{\boldsymbol{n}})$ is assumed to be the linear combination of $n_{\rm c}$ *components* $\{\mathsf{s}^i(\hat{\boldsymbol{n}})\}_{i=1,\cdots,n_{\rm c}}$ so that

$$T_\nu^{\rm obs}(\hat{\boldsymbol{n}}) = \mathcal{A}_{\nu i}\,\mathsf{s}^i(\hat{\boldsymbol{n}}) + \mathsf{n}_\nu(\hat{\boldsymbol{n}}), \tag{15}$$

where $n_\nu(\hat{\boldsymbol{n}})$ models the instrumental noise. The general idea subtending this algorithm is that the components, which result from completely different physical processes, have different spatial morphologies or structures. These morphological differences translate into a difference in their representation into a fixed

waveform dictionary $\mathcal{D}$. If only a few coefficients of a fixed dictionary are enough to completely represent a given component, this component is said to be sparse in that dictionary $\mathcal{D}$. The dictionary succeeds in catching the general features that characterize the component morphology. That is why separating the observed map into components that maximize their sparsity in a given dictionary is an efficient strategy to distinguish between physically different emission sources. In practice, a wavelet basis is a good choice for astrophysical components that overwhelmingly contain smooth spatial features. The GMCA is a sparsity-maximization algorithm, a notion that we briefly introduce below.

Let $\{\mathrm{d}^j(\hat{\boldsymbol{n}})\}$ be the set of vectors that forms the dictionary $\mathcal{D}$. Let $\alpha_{ij} = \langle \mathrm{s}^i(\hat{\boldsymbol{n}}), \mathrm{d}^j(\hat{\boldsymbol{n}})\rangle$ denote the scalar product coefficients between $\mathrm{s}^i(\hat{\boldsymbol{n}})$ and $\mathrm{d}^j(\hat{\boldsymbol{n}})$. When $\mathcal{D}$ is an orthogonal wavelet basis, the following properties hold

$$\begin{aligned}\langle \mathrm{d}^i(\hat{\boldsymbol{n}}), \mathrm{d}^j(\hat{\boldsymbol{n}})\rangle &= 0 \text{ if } i \neq j\\ \langle \mathrm{d}^i(\hat{\boldsymbol{n}}), \mathrm{d}^i(\hat{\boldsymbol{n}})\rangle &= 1\\ \mathrm{s}^i(\hat{\boldsymbol{n}}) &= \sum_j \langle \mathrm{s}^i(\hat{\boldsymbol{n}}), \mathrm{d}^j(\hat{\boldsymbol{n}})\rangle\, \mathrm{d}^j(\hat{\boldsymbol{n}}).\end{aligned}$$

Then GMCA estimates the components $\{\mathrm{s}^i(\hat{\boldsymbol{n}})\}$ and the mixtures weights $\{\mathcal{A}_{vi}\}$ by maximizing the sparsity of each component in $\mathcal{D}$. As advocated in Bobin et al. (2008), a good sparsity estimate is the sum of the absolute values of $\{\alpha_{ij}\}_{i,j}$. Maximizing the sparsity of the components is then equivalent to minimizing this sparsity measure. The model parameters are estimated by the GMCA as follows:

$$\min_{\{\mathrm{s}^i(\hat{\boldsymbol{n}})\},\{\mathcal{A}_{vi}\}} \sum_{ij} \left|\alpha_{ij}\right| \text{ s.t. } \left\|\mathrm{T}_v^{\mathrm{obs}}(\hat{\boldsymbol{n}}) - \mathcal{A}_{vi}\mathrm{s}^i(\hat{\boldsymbol{n}})\right\| < \epsilon, \tag{16}$$

where ϵ stands for the reconstruction error. The norm $\|\,.\,\|$ stands for the usual ℓ_2 norm

$$\left\|\mathrm{T}_v^{\mathrm{obs}}(\hat{\boldsymbol{n}}) - \mathcal{A}_{vi}\mathrm{s}^i(\hat{\boldsymbol{n}})\right\| = \sqrt{\sum_{v,i,\hat{\boldsymbol{n}}} (\mathrm{T}_v^{\mathrm{obs}}(\hat{\boldsymbol{n}}) - \mathcal{A}_{vi}\mathrm{s}^i(\hat{\boldsymbol{n}}))^2}. \tag{17}$$

The GMCA estimates the components $\{\mathrm{s}^i(\hat{\boldsymbol{n}})\}$, which have only a few significant coefficients $\{\alpha_{ij}\}$ in the dictionary; i.e. the components that are sparse in $\mathcal{D}$. Further technical details are given in Bobin et al. (2008).

For *Planck*, the parameter ϵ is chosen to be very small. In that case, the components $\{\mathrm{s}^i(\hat{\boldsymbol{n}})\}$ are estimated by applying the pseudo-inverse of the mixing matrix $\mathcal{A}$ to the observation channels $\{\mathrm{T}_v^{\mathrm{obs}}(\hat{\boldsymbol{n}})\}$:

$$\mathrm{s}^i(\hat{\boldsymbol{n}}) = \sum_v \mathcal{A}^+_{vi}\mathrm{T}_v^{\mathrm{obs}}(\hat{\boldsymbol{n}}), \tag{18}$$

where $\mathcal{A}^+_{vi}$ is the element at a position $\{i, v\}$ of the pseudo-inverse matrix of $\mathcal{A}$ defined as $\mathcal{A}^+ = \left(\mathcal{A}^{\mathrm{T}}\mathcal{A}\right)^{-1}\mathcal{A}^{\mathrm{T}}$. Interestingly, the contribution of the component separation is then linear. As a consequence, the noise perturbing each component can be accurately known. Furthermore, the linearity of the separation guarantees that the separation technique itself does not generate non-Gaussianity in an estimated CMB map. Only the residual terms coming from the other components can create non-Gaussian features in the CMB.

Another important consequence is that these properties give us a conservative method to estimate the point source residuals remaining within the CMB maps after foreground cleaning, as described below. Because each source has its own spectral property, component separation techniques fail at disentangling the point sources emission from the observed maps. As a result, point sources remain mixed with the other components and the precise amount of the point sources emission by observation channels that has leaked in each component, is determined by the coefficients of the mixing matrix. More formally, in order to estimate the point source residuals embedded in the foreground-cleaned CMB maps, quoted $\mathrm{s}^{\mathrm{ps}}(\hat{\boldsymbol{n}})$, one can apply Eq. (18) to the simulated point sources in the observation channels $\{\mathrm{T}_v^{\mathrm{ps}}(\hat{\boldsymbol{n}})\}$

$$\mathrm{s}^{\mathrm{ps}}(\hat{\boldsymbol{n}}) = \sum_v \mathcal{A}^+_{v0}\mathrm{T}_v^{\mathrm{ps}}(\hat{\boldsymbol{n}}), \tag{19}$$

where the elements $\{\mathcal{A}^+_{v0}\}$ form the column of the pseudo-inverse matrix that corresponds to the CMB component. Then the brighter point sources, which have been previously detected in the *Planck*-HFI channels, are masked out and the corresponding gaps are restored with an *inpainting* method. A detailed description of the mask and the restoration technique will be given below in Sect. 4. The final full-sky map we obtain is an estimate of the unresolved infrared point source residuals, which contaminate the CMB temperature map after component separation with the GMCA. This sky map was divided into patches of 12.5×12.5 square degrees with 50% overlapping. We formed a set of 300 point source residuals square maps by selecting the patches with a maximal 30% masked area.

We performed the component separation with the GMCA on Sets I-fg and II-fg, each of 300 simulated patches generated following our idealized *Planck* sky model and described in the previous Sect. 3.1. As an output of this process, we obtained two sets of 300 foreground-cleaned CMB temperature maps. Note that the GMCA achieves the extraction of the foreground components as well. Unresolved point source residuals are added to each map of these two sets. Below we will refer to the sets of lensed CMB maps with galactic dust, SZ effect and point source residuals after the GMCA component separation as to Sets I-GMCA and II-GMCA respectively.

3.3. CMB lensing reconstruction

Here we apply a discrete version of the quadratic estimator developed by Okamoto & Hu (Eq. (6)) on the different sets of simulated maps previously described, namely Sets I, I-GMCA, II and II-GMCA. We seek to assess the foreground residuals impact on our capability to reconstruct CMB lensing with *Planck*.

3.3.1. Testing the estimator performances

First we explicitly give the expression of the discrete quadratic estimator that we derive from Eq. (6):

$$\hat{\phi}_{\mathrm{TT}}(\boldsymbol{U}) = \frac{A_{\mathrm{TT}}(L)}{L^2\mathsf{A}} \sum_{\mathcal{D}_1\cap\mathcal{D}_2} \bar{T}(\boldsymbol{u}_1)\bar{T}(\boldsymbol{u}_2)F_{\mathrm{TT}}(\boldsymbol{u}_1,\boldsymbol{u}_2)\,, \tag{20}$$

where $\boldsymbol{U}$, $\boldsymbol{u_1}$ and $\boldsymbol{u}_2$ are wave-vectors related by $\boldsymbol{u_1} + \boldsymbol{u_2} = \boldsymbol{U}$ and A is the area of the sky patch considered. The sum is performed on the intersection of two disks $\mathcal{D}_1$ and $\mathcal{D}_2$. The former is the zero-frequency centered disk defined by $\Delta_1|\boldsymbol{u_1}| \leq L_{\max}$, where Δ_1 denotes the frequency interval in the Fourier space (i.e. the smallest nonzero positive frequency), which equals $2\pi/\sqrt{\mathsf{A}}$. The latter, namely $\mathcal{D}_2$, is also a disk of radius $L_{\max}$, but centered around $\boldsymbol{U}$. It is therefore defined by $\Delta_1|(\boldsymbol{u}_2 - \boldsymbol{U})| \leq L_{\max}$. The wave-vectors $\boldsymbol{u}_1$, $\boldsymbol{u}_2$ and $\boldsymbol{U}$ correspond to $\boldsymbol{k}_1/\Delta_1$, $\boldsymbol{k}_2/\Delta_1$ and $\boldsymbol{L}/\Delta_1$ respectively. The normalization $A_{\mathrm{TT}}(L)$ and the weighting function $F_{\mathrm{TT}}(\boldsymbol{u}_1,\boldsymbol{u}_2)$ are the discrete version of Eq. (9) and Eq. (10)

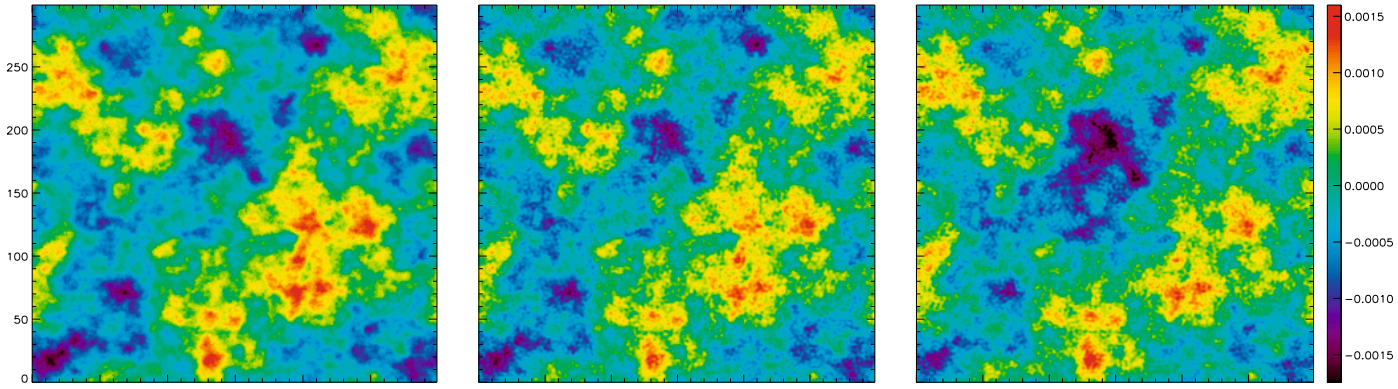

Fig. 2. Impact of the foregrounds residuals on the deflection field reconstruction on 12.5° × 12.5° square patches. *Left*: the input realization of the deflection amplitude; *middle*: the stack of 300 deflection estimates from the Set I maps (synthetic *Planck* temperature maps – without any foregrounds residuals); *right*: the stack of 300 deflection estimates from the Set I-GMCA maps (*Planck* temperature maps output of the GMCA component separation process). All maps have the same color table shown to the right of the figure.

respectively. For the *Planck*-HFI experiment, we verified that either cutting the sum in Eq. (20) at $L_{\rm max} = 2600$ or pushing it further leads to the same reconstructed potential field.

We studied our capability to reconstruct a map of the integrated potential field with the *Planck*-HFI idealized simulation, assuming a perfect component separation without any foreground residuals. We applied the discrete quadratic estimator on the Set I maps (see Sect. 3.1) to obtain 300 estimates of the same realization of the projected potential field ϕ. Once stacking these estimates, the final ϕ map is an estimate of the input ϕ realization. Following Hu (2001b), we prefer to present our results in terms of the deflection field amplitude rather than the very smooth gravitational potential field, to highlight the intermediate angular scales features. Figure 2 shows the input deflection field realization, which was used to simulate the lensing effect in the Set I maps (on the first panel), as well as its reconstruction with the quadratic estimator applied on the Set I maps (second panel). Even if the reconstruction noise is visible at smaller angular scales, the features of the deflection map are well recovered.

Characterizing *Planck* sensitivity to the projected potential APS requires us to account for both the CMB and the projected potential field cosmic variances. Thus, we moved on to Set II. As before we applied the quadratic estimator (Eq. (20)) on the lensed CMB maps to reconstruct projected potential fields. Averaging over the APS of these individual ϕ field estimates gave an evaluation of the quadratic estimator variance (as defined in Eq. (11)). The final reconstructed projected potential APS was obtained by subtracting the noise contributions, described in Sect. 2, from the variance. The former is related by Eq. (3) to the deflection APS shown in the Fig. 3. The error bars were estimated as the dispersion between each individual deflection APS reconstruction. Thus the Set II maps, which are idealized versions of the *Planck*-HFI sky assuming a perfect component separation, lead to a good reconstruction of the deflection APS up to $L_{\rm max} = 2600$. The error-bars evaluated here give an upper limit of the *Planck*-HFI sensitivity to the deflection APS. As one can see in Fig. 4, they are compatible with the theoretical 1σ error-bars one can calculate from the Fisher formalism

$$\Delta C_L^{\rm dd} = \sqrt{\frac{1}{N_{\rm eff}}}\left(C_L^{\rm dd} + N_L^{\rm dd}\right), \qquad (21)$$

where $N_{\rm eff} = 4\pi/L\Delta L\Delta$ is a naive estimate of the independent available Fourier modes. The error bars estimated here will provide us with a comparison level to quantify the impact of the foreground residuals.

3.3.2. Impact of the foreground residuals

Here we essentially redo the same analysis, but with the full-simulation pipeline of our *Planck*-HFI demonstration model. The integrated potential field is extracted from the Sets I-GMCA and II-GMCA described in Sect. 3.2.

First, we aim at developing an intuition for the impact of foreground residuals on the deflection map reconstruction. We used the Set I-GMCA, in which both deflection field and foreground realizations are fixed. As previously, the 300 deflection field estimates reconstructed with the quadratic estimator were stacked to produce a unique reconstructed deflection field shown in Fig. 2. We can see that the recovery of the underlying deflection field is still achieved even with foregrounds emission and after the GMCA. The impact of the foreground residuals is nevertheless visible, mostly at angular scales larger than 2 degrees, whereas the intermediate angular scale features seem more preserved.

For a more quantitative analysis, we moved on to the impact of the foreground residuals on the deflection APS reconstruction. We used the Set II-GMCA (see Sects. 3.1 and 3.2) to ensure that the variances of the CMB, the deflection field and the foregrounds were accounted for. We reconstructed a deflection field estimate from each of the Set II-GMCA maps with the quadratic estimator given in Eq. (20). Finally, we obtained the reconstructed deflection APS from the average variance over these 300 deflection APS estimates as described in Sect. 3.3.1.

The reconstructed binned deflection APS with the evaluated 1σ errors is represented in Fig. 3. Figure 4 shows the difference between the reconstructed and the input deflection APS. First we report that the foreground residuals do not compromise the *Planck*-HFI capability to reconstruct the deflection APS – or equivalently the integrated potential APS. Figure 3 shows that the APS reconstruction is preserved at the angular scales from $L = 60$ up to $L = 2600$. In this multipole range, the GMCA algorithm succeeds in letting the statistical properties of the lensed CMB temperature anisotropies unchanged, which suggests that this is a well-appropriated component separation tool for CMB lensing reconstruction. As for the first multipole bin, we report a 4σ excess of the deflection signal in the $L = 2$ to $L = 60$ multipole range. We checked that this bias is linked to

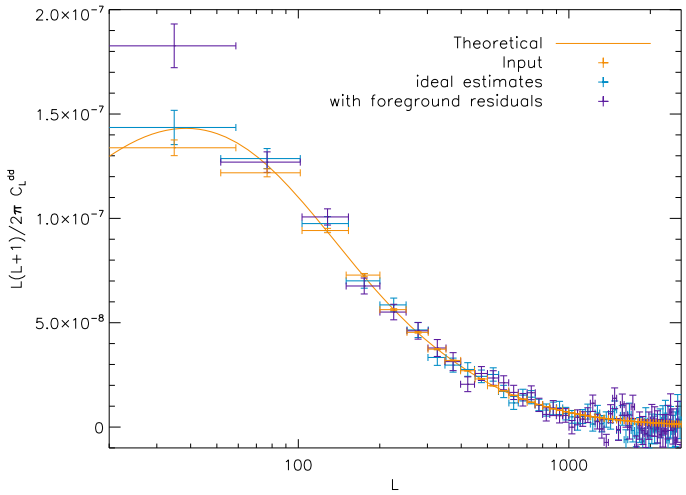

Fig. 3. Deflection APS. Data-points are the binned APS reconstructed from *Planck* synthetic lensed CMB maps in two cases: (light blue/grey) the *ideal* case without any foreground and (dark blue/black) the case with foreground residuals from the GMCA output CMB maps. The fiducial deflection APS calculated with CAMB is figured by the (orange/solid) line; the orange/grey data points are the binned deflection APS estimates on the 300 input deflection field realizations. The horizontal and vertical intervals associated with the data points represent the averaging multipole bands and the 1σ errors respectively.

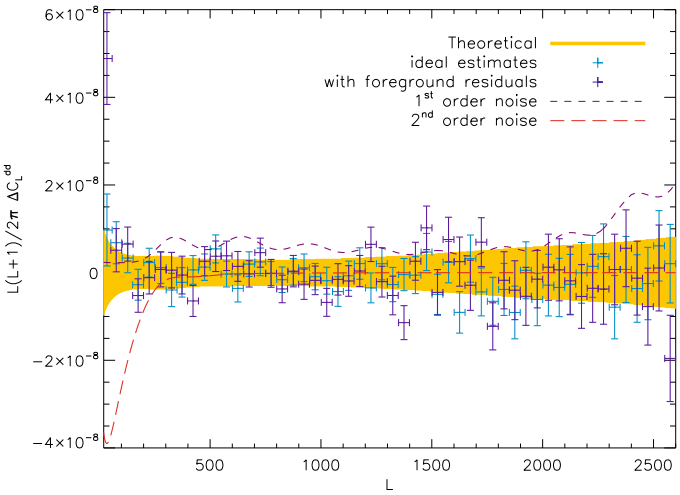

Fig. 4. Residual bias of the deflection APS reconstruction. Data-points figure the difference between the reconstructed and the input deflection APS averaging over 300 estimates: in the *ideal* case in light blue/grey and in the case with foreground residuals in dark blue/black (consistent with the Fig. 3 caption). The lines show the non-Gaussian noise terms of the quadratic estimator at the first-order (violet/dashed) and at the second-order (red/long dashed) in $C_L^{\rm dd}$. The orange/grey colored band is the analytical 1σ error band derived from the Fisher formalism.

the introduction of the unresolved point source residuals in our simulation pipeline. Interestingly, we found that this excess originates not in the level of residuals themselves, but mostly in the cutting procedure[4] we used to extract the set of 300 square maps from our full-sky point source residuals. We postpone a closer inspection of the low multipole lensing reconstruction behavior to the complete full-sky study (below in Sect. 4). Apart from the excess signal in the first bin, the impact of the foreground residuals on the deflection reconstruction is also slightly visible at all angular scales, as seen in the Fig. 4. If the difference between reconstructed and input APS is still compatible with zero within the theoretical 1σ errors in the 60 to 2600 multipole range, this residual bias appears more featured, more oscillating than in the previous no-foreground-case.

To quantify this degradation in the deflection APS reconstruction, we calculated the total error in unit of σ, defined as

$$\Delta = \sum_b \left| \frac{\hat{C}_b^{\rm dd} - C_b^{\rm dd}}{\sigma_b} \right|, \qquad (22)$$

where $\hat{C}_b^{\rm dd}$ and $C_b^{\rm dd}$ are respectively the reconstructed and input deflection APS in the b frequency band, and σ_b the 1σ error on $\hat{C}_b^{\rm dd}$. Note that when evaluating the total error, we excluded the first bin bias, which has been discussed previously. With this definition we found a total error, $\Delta_{\rm ideal} = 33$, in the no-foreground case whereas $\Delta_{\rm gmca} = 41$, for GMCA foreground residuals. If the total error serves as quantifying the increase of the *bias* of the deflection APS reconstruction, one can also evaluate the increase of the *errorbars*. We found that foreground residuals result in a 10% increase of the errorbars on average. This suggests that at least an amount of the non-Gaussian foreground residuals is mixed up with the lensing signal in the reconstruction process. Foregrounds showing some small angular scale (around 15 to 5 arcmin) features – like concentrated dust emission or brightest SZ clusters and point sources smeared by the instrument beam function – are potentially more challenging for the CMB lensing reconstruction. In addition, we remind that our sky model is intended to catch the dominant foreground features at the *Planck*-HFI frequencies. The sub-dominant existing emissions, as free-free or synchrotron emissions, may marginally degrade our results as they are expected to slightly increase the foreground residuals whithin the CMB map.

As a final remark we note that because of the first bin excess signal problem, which is linked to the sphere to patches transition, one might prefer a full-sky approach when seeking a precise lensing reconstruction at the higher ($L < 60$) angular scales.

4. Impact of masks on the full-sky lensing reconstruction

4.1. Introduction

From now on, we move to a full-sky analysis of the CMB lensing effect. Some large areas of the map, where the CMB signal is highly dominated by the foreground emission (e.g. the galactic plane, the point source directions), have to be masked out. Cutting to zero introduces some mode-coupling within the CMB observables. As the lensing reconstruction methods rely on the off-diagonal terms of the CMB data covariance matrix, the map-masking yields some artifacts in the projected potential estimate if not accounted for. Several methods have been proposed to treat the masking effect for extracting the lensing potential field from the WMAP data. In Smith et al. (2007), the reconstruction is performed on the least-square estimate of the signal given the all-channels WMAP temperature data, requiring the inversion of the total data covariance matrix ($S+N$). However, relying at least on the inversion of the noise covariance matrix, such an optimal

[4] The cutting procedure involves a sphere-to-plan projection, an apodization and a fit of the Fourier coefficients of the square map. From the tests we run (not presented here), the apodization appears to have the most harmful impact on the high angular scale deflection reconstruction. A complete study of the impact of the sphere to patches transition will be the subject of a companion paper.

data filtering approach is very CPU-consuming when applied to the WMAP maps. The *Planck*-HFI provides 50 Mega pixels maps. Thas is why the previous method to account for the masking will be difficult to extend to *Planck*. In Hirata et al. (2008), the need for dealing with the noise covariance matrix is avoided by cross-correlating different frequency band maps. However, this method implies that no component separation has been performed on the CMB maps before the lensing extraction. As a result, a lot of non-Gaussianities of foreground emission origin yield some artifact in the projected potential estimate, requiring a challenging post-processing to be corrected out. As previously mentioned, the *Planck* collaboration devotes considerable effort in the component separation activities, and the currently developed methods have already proved their efficiency (Leach et al. 2008). Moreover, the results we obtained with the *demonstration analysis* (see Sect. 3) tend to indicate that the lensing reconstruction is still doable after a component separation. Hence we plan to exploit the *Planck* frequency band maps to clean out the foreground emission before reconstructing the lensing potential rather than using the cross-correlation based lensing estimator. As a consequence, we need an alternative method to solve the masking issue in maps at the *Planck* resolution. Here we propose to use an *inpainting* method, assess its impact on the CMB lensing retrieval and check its robustness to the presence of foregrounds residuals within the CMB map.

First, we describe the hypothesis assumed and the tools we use to generate synthetic all-sky lensed temperature maps for *Planck*. Then we describe our full-sky lensing estimator and test its performances on some *Planck*-like temperature maps. Finally, we review the *inpainting* method and conclude in studying the effect of the *inpainting* on the projected potential APS reconstruction in two cases, first assuming a perfect component separation, then with point source residuals.

4.2. Full-sky simulation

The formalism reviewed in Sect. 2 is almost fully applicable to the spherical case. In particular the remapping equation (Eq. (1)) still holds, so that a lensed CMB sphere is given by

$$\widetilde{T}(\hat{\boldsymbol{n}}) = T(\hat{\boldsymbol{n}} + \nabla\phi(\hat{\boldsymbol{n}})), \tag{23}$$

where the ∇ operator is to be understood as the covariant derivative on the sphere (Lewis & Challinor 2006). $\nabla\phi$ is identified to be the deflection field $\boldsymbol{d}$. Its zenithal and azimuthal coordinates can be calculated as the real and imaginary parts of a complex spin one field, using spin-weighted spherical harmonics transform – the detailed calculation can be found in Hu (2000) and Lewis (2005).

The LensPix[5] package described in Lewis (2005) aims at generating a set of lensed CMB temperature and polarization maps from the analytical auto- and cross-APS of $\{T, E, B, \phi\}$, the temperature, the E and B polarization modes and the line-of-sight projected potential respectively. The maps are provided in the HEALPix[6] pixelization scheme (Górski et al. 2005). The CMB lensing simulation is achieved in remapping the anisotropy fields according to Eq. (23) of a higher resolution map using a bi-cubic interpolation scheme in equi-cylindrical pixels. A lensed temperature map at the *Planck* resolution (nside = 2048) can be computed in about five minutes on a 4-processors machine. The relative difference between the lensed temperature APS reconstructed on such a map and the lensed APS analytically obtained with CAMB[7] (Lewis et al. 2000) is below 1% up to $l = 2750$. Here, to conservatively ensure a relative error below 1%, we choose a multipole cut at $L_{\max} = 2600$. By its speed and precision quality, LensPix is a well-adapted tool for a CMB lensing analysis with *Planck* data alone.

We obtained some *Planck*-HFI synthetic maps as in the flat-sky case (see Sect. 3). White Gaussian noise realizations and Gaussian beam effect were added to the lensed temperature maps provided by the LensPix code. This Gaussian noise contribution is fully defined by the all-channels beam-deconvolved APS given by

$$N_l^{\mathrm{TT}} = \left(\sum_{\nu} \frac{1}{N_l^{\mathrm{TT},\nu}} \right)^{-1}, \tag{24}$$

where $N_l^{\mathrm{TT},\nu} = (\theta_{\mathrm{fwhm}}\,\sigma_T)^2 \exp\left[l(l+1)\theta^2_{\mathrm{fwhm}}/8\ln 2 \right]$, θ_{fwhm} and σ_{T} are the FWHM and the level of white noise per resolution element respectively, as given in Table 1. The noise map was generated with the map-creation tool of the HEALPix package.

For the lensing reconstruction analysis we prepared two sets of 50 all-sky maps with 1.7 arcmin of angular resolution (the HEALPix resolution parameter nside = 2048). In each set, maps are the *lensed* CMB temperature plus the *Planck*-HFI nominal Gaussian noise.

4.3. Full sky lensing reconstruction

We carried out an integrated potential estimation tool based on the full-sky version of the quadratic estimator derived in Hu (2001a). We closely followed the prescription given in Okamoto & Hu (2003) to build an efficient estimator, so that

$$\widehat{\phi}_{LM} = \frac{N_L^{(0)}}{L(L+1)} \int \mathrm{d}\hat{\boldsymbol{n}} \left(T^{(hp)}(\hat{\boldsymbol{n}}) \boldsymbol{\nabla} T^{(w)}(\hat{\boldsymbol{n}}) \right) \cdot \boldsymbol{\nabla} Y^*_{LM}(\hat{\boldsymbol{n}}), \tag{25}$$

where $T^{(\mathrm{hp})}$ and $T^{(\mathrm{w})}$ are respectively high-pass filtered and weighted lensed CMB temperature field, given by

$$\begin{aligned} T^{(\mathrm{hp})}(\hat{\boldsymbol{n}}) &= \sum_{lm} \frac{1}{\bar{C}_l^{\mathrm{TT}}} \bar{T}_{lm} Y_{lm}(\hat{\boldsymbol{n}}) \\ T^{(\mathrm{w})}(\hat{\boldsymbol{n}}) &= \sum_{lm} \frac{C_l^{\mathrm{TT}}}{\bar{C}_l^{\mathrm{TT}}} \bar{T}_{lm} Y_{lm}(\hat{\boldsymbol{n}}). \end{aligned} \tag{26}$$

The covariant derivative operator $\boldsymbol{\nabla}$ applied on the spherical harmonics can be expressed in terms of the spin ± 1 projectors $e_\pm = e_\theta \pm i e_\phi$ and the spin weighted spherical harmonics, as explained in Okamoto & Hu (2003). The quantities appearing in Eq. (25) can thus be calculated by direct and inverse (spin zero) spherical harmonics and spin-weighted (spin ± 1) spherical harmonics transforms. As for the estimator normalization, quoted $N_L^{(0)}$, it is the same as the Gaussian contribution to the estimator variance. For its expression, we refer to Eq. (34) in Okamoto & Hu (2003).

Then, extending to the spherical case the calculations reviewed in Sect. 2, the covariance of the integrated potential field estimator $\widehat{\phi}_{LM}$, averaged over an ensemble of CMB and gravitational potential field realizations, depends on the potential APS, so that

$$\langle \widehat{\phi}^*_{LM}\, \widehat{\phi}_{L'M'} \rangle = \delta_{LL'}\delta_{MM'} \left(C_L^{\phi\phi} + N_L^{(0)} + N_L^{(1)} + N_L^{(2)} \right), \tag{27}$$

[5] http://cosmologist.info/lenspix/

[6] The acronym for "Hierarchical Equal Area isoLatitude Pixelization" of a sphere (see http://healpix.jpl.nasa.gov/index.shtml).

[7] The "Code for Anisotropies in the Microwave Background" is a so-called Boltzmann's code described at http://camb.info/

where $N_L^{(0)}$, $N_L^{(1)}$ and $N_L^{(2)}$ are zeroth, first and second order in $C_L^{\phi\phi}$ noise terms respectively. To calculate the first sub-dominant noise term, one can use the expression derived in the flat-sky approximation by Kesden et al. (2003). Likewise, the second order term is given in Hanson et al. (2010). As these terms are one order of magnitude smaller than the dominant $N_L^{(0)}$ term and because the flat-sky approximation is known to be robust for the potential estimator noise calculation (Okamoto & Hu 2003), we assumed and verified that the deviation due to the flat-sky approximation is negligible.

Within the framework of Monte-Carlo analysis, we built a projected potential APS estimator so that

$$\widehat{C}_L^{\phi\phi} = \frac{1}{N}\sum_{i=1}^{N}\left[\frac{1}{2L+1}\sum_M |\widehat{\phi}^i_{LM}|^2\right] - (N_L^{(0)} + N_L^{(1)} + N_L^{(2)}), \quad (28)$$

where $\widehat{\phi}^i_{LM}$ is the integrated potential field estimate on the ith CMB temperature realization, $i \in \{1, \ldots N\}$. Note that since $N_L^{(1)}$ and $N_L^{(2)}$ depend on the potential APS itself, it should be evaluated and subtracted iteratively. Here we calculate it once from the theoretical integrated potential APS.

Finally, we tested our APS estimator on a set of 10 lensed CMB temperature maps of 50 millions of pixels, including the nominal *Planck* noise, generated as described in Sect. 4.2. As in the flat-sky case, sums in the spherical harmonic space were cut at $L_{\max} = 2600$. The results, compiled in the form of an integrated potential APS estimate averaged over the 10 trials (see Eq. (28)), are shown in the left panels of Fig. 6.

4.4. Inpainting the mask

We took into account the cutting effect of the temperature map before any lensing reconstruction rather than making any changes in the quadratic estimator (given in Eq. (25)) to account for the mask. This approach was motivated by the high quality and the large frequency coverage of the *Planck* data, which allow one to reconstruct the CMB temperature map on roughly 90% of the sky. It therefore suggests that a method intended to fill the gap in the map can be applicable.

Several methods, which are referred to as *inpainting*, were recently developed since the pioneering work of Masnou & Morel (1998). The general purpose of these methods is to restore missing or damaged regions of an image to retrieve the original image as far as possible. For the CMB lensing reconstruction, the ideal *inpainting* method would lead a restored map with the same statistical properties as the underlying unmasked map. To use a notion briefly mentioned in Sect. 3.2, the masking effect can be thought of as a loss of *sparcity* in the map representation: the information required to define the map has been spread across the spherical harmonics basis. That is the reason why the *inpainting* process can also be thought of as a restoration of the CMB temperature field *sparcity* in a conveniently chosen waveform dictionary.

Elad et al. (2005) introduced a sparsity-based technique to fill in the missing pixels. This method was extended to the sphere in Abrial et al. (2008, 2007). In a nutshell, the masked CMB map is modeled as follows:

$$\mathcal{T}(\hat{\boldsymbol{n}}) = \mathcal{M}(\hat{\boldsymbol{n}})T(\hat{\boldsymbol{n}}), \quad (29)$$

where $\mathcal{M}(\hat{\boldsymbol{n}})$ stands for a binary mask, the entries of which are one when the pixel is observed and zero when it is missing. As emphasized in Elad et al. (2005); Abrial et al. (2008), if $T(\hat{\boldsymbol{n}})$ has a sparse representation in a given waveform dictionary $\mathcal{D}$ (see Sect. 3.2), masking is likely to degrade the sparsity the CMB map in $\mathcal{D}$. Let $\{d^j(\hat{\boldsymbol{n}})\}$ be the set of vector that forms the dictionary $\mathcal{D}$. Let α_j denote the scalar product (so-called coefficients) between $T(\hat{\boldsymbol{n}})$ and $d^j(\hat{\boldsymbol{n}}) : \alpha_j = \langle T(\hat{\boldsymbol{n}}), d^j(\hat{\boldsymbol{n}})\rangle$. For the sake of simplicity, we further assume the set $\{d^j(\hat{\boldsymbol{n}})\}$ forms an orthonormal basis. Recovering the missing pixel can then be made by a solution that minimizes the sparsity of the $\mathcal{T}(\hat{\boldsymbol{n}})$ in $\mathcal{D}$. As in Sect. 3.2, an appropriate sparsity estimate of $\mathcal{T}(\hat{\boldsymbol{n}})$ in $\mathcal{D}$ consists in measuring the sum of the absolute values of $\alpha_j = \langle \mathcal{T}(\hat{\boldsymbol{n}}), d^j(\hat{\boldsymbol{n}})\rangle$. The recovered CMB map is then obtained by solving the following optimization problem:

$$\min_{\{\mathcal{T}(\hat{\boldsymbol{n}})\}} \sum_j |\langle \mathcal{T}(\hat{\boldsymbol{n}}), d^j(\hat{\boldsymbol{n}})\rangle| \text{ s.t. } \|\mathcal{T}(\hat{\boldsymbol{n}}) - \mathcal{M}(\hat{\boldsymbol{n}})T(\hat{\boldsymbol{n}})\| < \epsilon, \quad (30)$$

where ϵ stands for the reconstruction error. It has been shown in Abrial et al. (2008) that this inpainting technique leads to very good CMB recovery results. Our inpainting algorithm can be found in Abrial et al. (2007, 2008) and its implementation is based on the multi-resolution on the sphere (MRS) package[8]. Below we seek to assess the impact of the *inpainting* mask correction in *Planck*-like maps on a CMB lensing reconstruction.

4.5. Effect of inpainting

First we have to choose a realistic mask, which could also be applied to the forthcoming *Planck* temperature map. However, depending on the details of the component separation pipeline the different methods developed in the *Planck* consortium (see Leach et al. 2008) yield slightly different masks. Furthermore, the mask size is not a necessary criteria for the final choice of the component separation method that will be selected for the *Planck* data analysis. We thus adopt a conservative approach, which consists in choosing the union of the masks provided by each of the methods at the time of the component separation *Planck working group* second challenge (Leach et al. 2008). This mask, hereafter referred to as the *union mask*, rejects about 11% of the sky, as shown in Fig. 5.

Then the 10 *Planck*-like lensed CMB temperature maps we generated (see Sect. 4.2) were masked according to the *union mask* and then restored by applying the *inpainting* method described in Abrial et al. (2008). From each of these mask-corrected maps we extracted a projected potential field using the quadratic estimator of Eq. (25). As previously, the results were compiled in the form of the average projected potential APS $\widehat{C}_L^{\phi\phi}$ following Eq. (28). The reconstructed deflection APS, given by $\widehat{C}_L^{\rm dd} = L(L+1)\widehat{C}_L^{\phi\phi}$, as well as the bias between estimated and fiducial deflection APS $\Delta C_L^{\rm dd}$ are shown in the right panels of Fig. 6.

We found that the mask corrected by the inpainting results in a marginal increase (~4%) of the 1σ errors on the estimated deflection APS (hence on the projected potential APS). Masking and inpainting causes an increase of the reconstructed APS bias $\Delta C_L^{\rm dd}$ arising mostly at large angular scale corresponding to multipole $L < 300$. However, this bias is weaker than the sub-dominant second-order in $C_L^{\phi\phi}$ non-Gaussian bias. Figure 6 shows a clear increase of power in the very first multipole band ($2 < l < 10$). In this multipole range, *Planck* is not expected to achieve a good reconstruction of the potential APS (Hu & Okamoto 2002). From the multipole $L = 300$ up to $L = 2600$, the bias stays below the first-order in $C_l^{\phi\phi}$ non-Gaussian bias and

[8] http://jstarck.free.fr/mrs.html

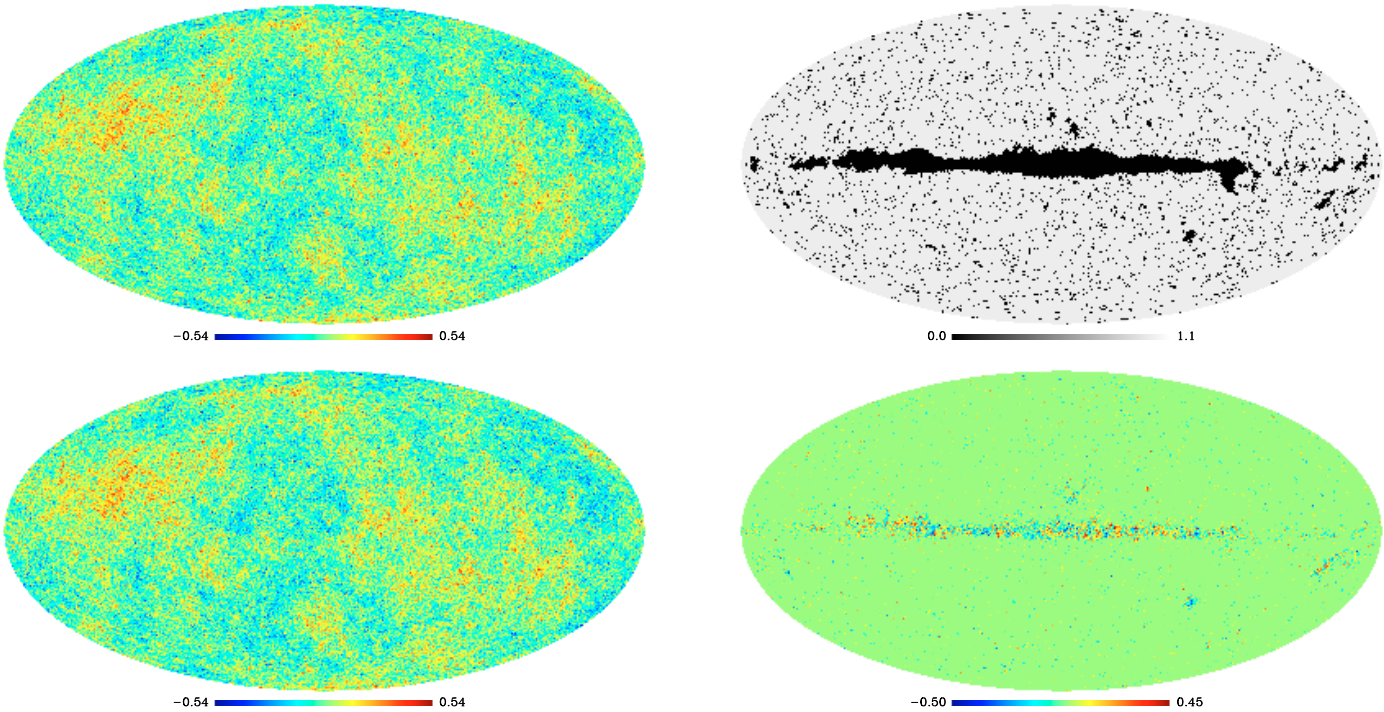

Fig. 5. All-sky maps in Galactic Mollweide projection. *Upper panels*: (*left*) a *Planck*-HFI synthetic CMB temperature map in milliKelvin, (*right*) the union mask defined in Sect. 4.5. The grey region shows the observed pixels, whereas the rejected ones are in black. *Lower panels*: left panel shows the restored CMB map obtained by applying the *inpainting* process (described in Sect. 4.4) on the previous upper-left CMB map masked according to the union mask and the right panel shows the difference between the input (upper-left) CMB map and the restored (lower-left) one.

is compatible with the theoretical 1σ errors expected for the quadratic estimator. From fully controlling the inpainting impact, one might want to push further the study by analytically calculating or Monte-Carlo estimating the mask induced bias. However, it is not mandatory for reconstructing the projected potential APS with *Planck*. The masking effect, once corrected by inpainting, becomes a sub-dominant systematic effect that can be safety neglected.

4.6. Robustness against the unresolved point sources

Up to now, we handled two important issues linked to the presence of foreground emissions in the observation maps independently, the impact of the foreground residuals after component separation with GMCA in Sect. 3.3 and the impact of the masking corrected with the inpainting method in the previous subsection (Sect. 4.5). We found that none of them compromises our ability to reconstruct the deflection APS. In a more realistic approach, these two issues should be handled together, as the inpainting process is intended to be applied on a CMB map contaminated by foreground residuals. Foreground residuals are likely to harden the inpainting process and consequently degrade the CMB lensing recovery. Here we assess the robustness of the deflection reconstruction on masked and inpainted CMB maps when adding infra-red point source residuals. This choice was made for two reasons. The point source residuals after component separation are a well-known matter of concern in any CMB non-Gaussianities analysis and the emission of the infra-red sources population is one of the major foreground contaminants at the *Planck*-HFI observation channels.

We used the full-sky map of infra-red point source residuals after a component separation with the GMCA, which we had estimated in Sect. 3.2. Thess point source residuals were added to the 10 synthetic *Planck*-lensed CMB temperature maps described in Sect. 4.2. Then we repeated the same analysis as previously in Sect. 4.5: the *union mask* was applied to the maps, cutting out the brightest infra-red sources, which were detected during the Component Separation *Planck working group* second challenge (Leach et al. 2008). The 10 masked maps were restored with the *inpainting* method before being ingested in the full-sky quadratic estimator of the projected potential field. The results of the whole analysis are presented in the form of the average reconstructed deflection APS and bias in Fig. 7.

We found that the inpainting performances were only marginally degraded (at $\leq 1\sigma$ level) by the point source residuals within the CMB maps, and this degradation occured mainly at the two multipole extremes. At the lower multipoles ($L < 30$), the APS deflection reconstruction suffers from a 1σ increase of the bias, whereas at the higher multipoles, only the error bars increase. We conclude that the inpainting method succeeds in keeping the statistical properties of the CMB map unchanged even with highly non-Gaussian foreground residuals and is a qualified method to handle the masking issue when seeking a CMB lensing recovery. In addition, the results compiled in the Fig. 7 give the total impact of point sources on the deflection reconstruction, as they account for both the masking of the bright detected sources and the unresolved residuals. We report that point sources are responsible for a total 13% increase of the 1σ errors on the reconstructed APS deflection, mainly induced by the unresolved residuals. As a summary, the major nuisance of point sources is related to the masking of the bright ones, which

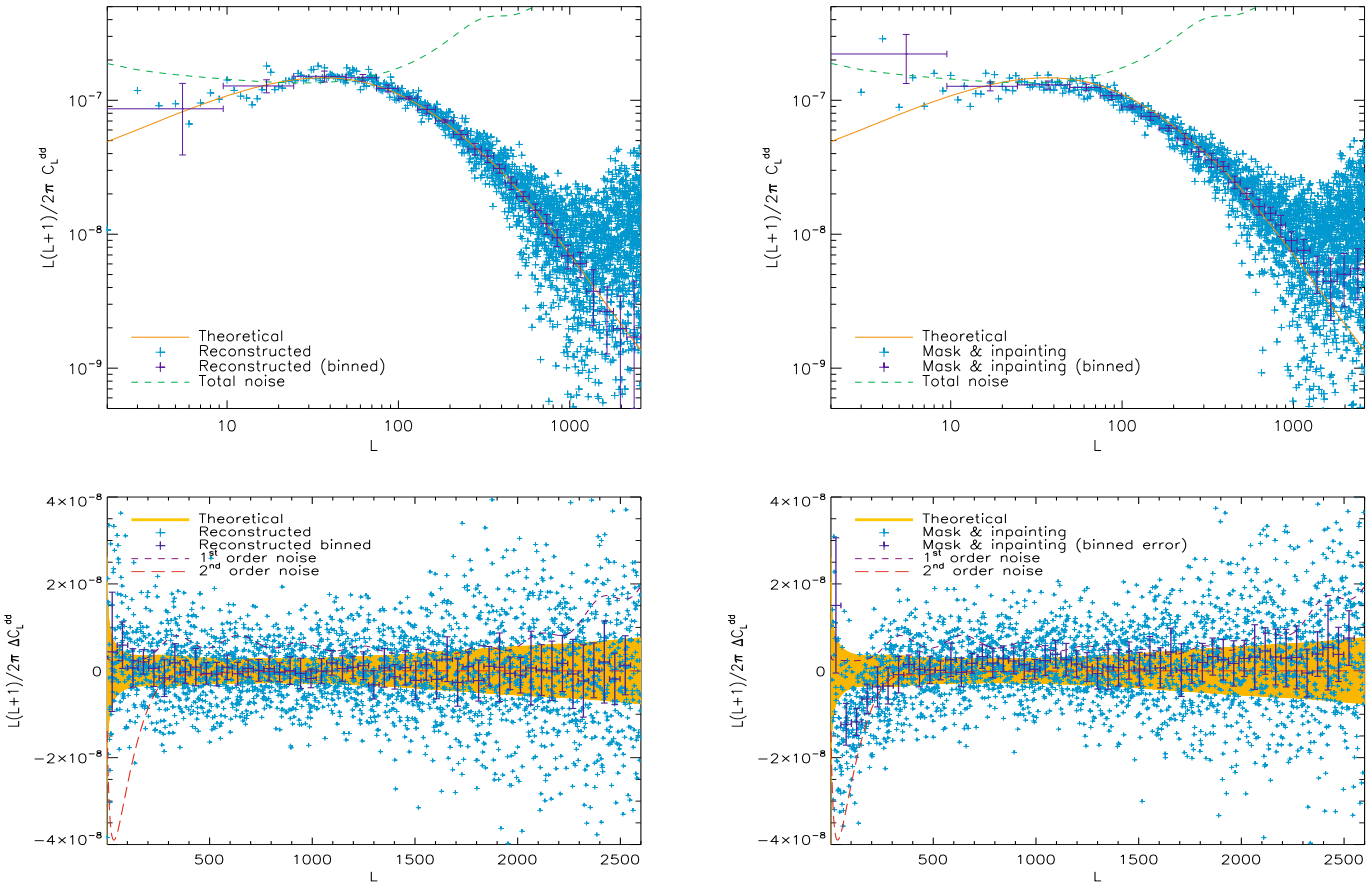

Fig. 6. Impact of the masking corrected by an *inpainting* process. The left panels are for the full-sky *Planck* synthetic lensed temperature maps, whereas the right panels compile the results drawn from the masked lensed temperature maps restored with the *inpainting* process described in Sect. 4.4. *Upper panels*: the reconstructed deflection APS $\widehat{C}_L^{\rm dd}$, obtained from the projected potential APS estimate of Eq. (28). The (light blue/grey) crosses show the $\widehat{C}_L^{\rm dd}$ per multipole and the (dark blue/black) data points are the band-power $\widehat{C}_L^{\rm dd}$. The horizontal intervals represent the averaging multipole bands, and the vertical ones the 1σ error. The (orange solid) line figures the fiducial deflection angle APS $C_L^{\rm dd}$, and the (green dashed) line the total noise of the quadratic estimator ($N_L^{(0)}+ N_L^{(1)} + N_L^{(2)}$). *Lower panels*: the bias of the deflection APS reconstruction $\Delta C_L^{\rm dd}$ defined as the difference between the reconstructed deflection APS $\widehat{C}_L^{\rm dd}$ and the input deflection APS $C_L^{\rm dd}$. Consistently with the upper panels, (light blue/grey) crosses are $\Delta C_L^{\rm dd}$ per multipole, and (dark blue/black) data points are the band power $\Delta C_L^{\rm dd}$ with the associated averaging multipole widths (horizontal intervals) and 1σ error (vertical intervals). The large (orange/grey) band shows the analytical $\pm 1\sigma$ errors per band power expected for the quadratic estimator (see Eq. (21)). Finally, the lines show the non-Gaussian sub-dominant noise terms at the first-order (violet/dashed) and at the second-order (red/long dashed) in $C_L^{\phi\phi}$.

tend to increase the bias on the reconstructed deflection APS, whereas the unresolved residuals result mainly in an increase of the errors on the deflection retrieval.

Conclusions

The High Frequency Instrument (HFI) of the *Planck* satellite, which was launched on the 14th of May 2009, has the sensitivity and the angular resolution required to allow a *reconstruction* of the CMB lensing using the temperature anisotropies map alone. The pioneer works to put evidence of the CMB lensing within the WMAP data are not directly applicable or not well-optimized to the *Planck* data. First, one might want to take advantage of the efficient component separation algorithms developed for *Planck* before applying a CMB lensing estimator rather than to correct the lensing reconstruction from the bias due to the foreground emission afterward. Second, we need an efficient and manageable method to take into account the sky cutting within the 50 Mega-pixels maps provided by *Planck*. In addition, the CMB lensing is related to another imminent problem: characterizing the non-Gaussianities of the temperature anisotropies (primordial non-Gaussianities, cosmic string, etc.).

We implemented both the flat-sky and the all-sky versions of the quadratic estimator of the projected potential field described in Hu (2001b); Okamoto & Hu (2003) to apply them to *Planck* synthetic temperature maps. First, we prepared a *demonstration model* within the flat-sky approximation, which consists in running the GMCA, a component separation method described in Bobin et al. (2008), on *Planck* frequency channel synthetics maps, containing the lensed CMB temperature, the *Planck* nominal instrumental effects (modeled by a white Gaussian noise and a Gaussian beam) and the three dominant foreground emissions at the *Planck*-HFI observation frequencies, namely the SZ effect, the galactic dust and the infra-red point sources. We performed a Monte-Carlo analysis to quantify the impact of the foreground residuals after the GMCA on the projected potential field and APS reconstructions. Then we moved on to the full-sky case, using the LensPix algorithm (Lewis 2005) to generate lensed

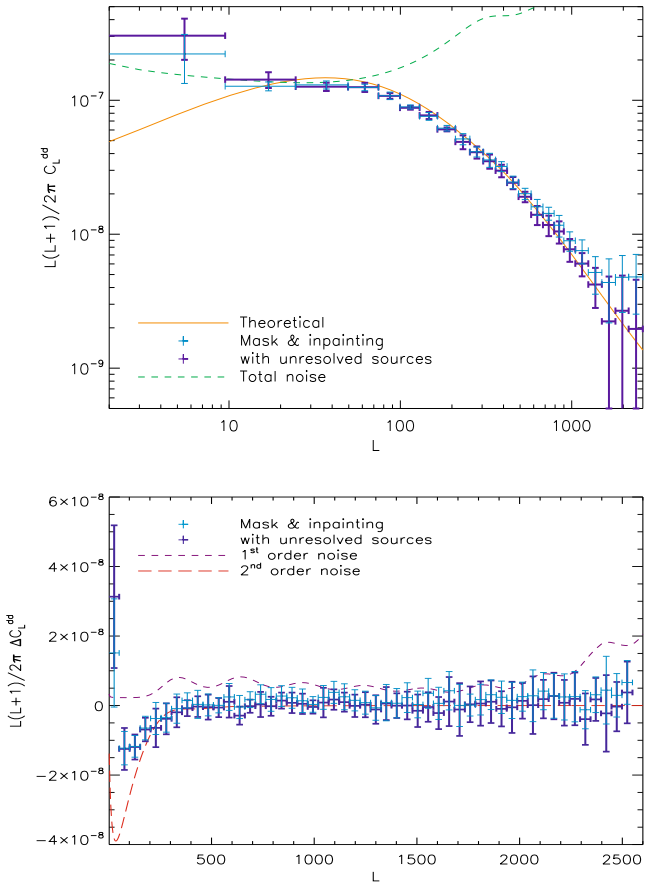

Fig. 7. Robustness of the inpainting to the unresolved point sources. The upper panel shows the reconstructed deflection APS, whereas the lower panel the bias on the deflection APS reconstruction. The (dark blue/black) data points show the result of the full-sky quadratic estimation on the set of lensed CMB maps with point source residuals, which were masked and then restored with the inpainting technique, as described in Sect. 4.6. For comparison the results obtained in Sect. 4.5 in the case without any sources residuals, are shown here as (light blue/grey) crosses. The fiducial analytical deflection APS as well as the total reconstruction noise and the two APS bias are shown following the same representation code as in Fig. 6, and horizontal and vertical intervals have the same meaning as described in the Fig. 6 caption. For clarity only the *band power* reconstructed APS and APS bias are represented, and the theoretical error bars by multipole bins are not shown.

CMB temperature maps at the *Planck* resolution. We performed a Monte-Carlo analysis to tackle the masking issue; we used the *inpainting* method described in Abrial et al. (2008) to restore the *Planck* synthetic temperature maps, masked according to a realistic cut out of 11% of the sky, accounting for the bright detected point sources. By applying the projected potential quadratic estimator on these restored maps, we studied the impact of the inpainting of the mask on the *Planck* sensitivity to the projected potential APS. Finally, we assessed the total impact of the point sources emission, in confronting the inpainting method with the unresolved point source residuals.

Results

1. Within our flat-sky *demonstration model*, we found that the reconstruction of the projected potential field is still feasible after a component separation with the GMCA. More quantitatively, the foreground residuals in the GMCA output CMB maps lead to a 10% increase of the 1σ errors on the projected potential APS reconstruction when applying the quadratic estimator. The GMCA process results in an increase of the dispersion of the projected potential APS reconstruction, but this dispersion remains within the theoretical 1σ errors at all angular scales but the $L < 60$ multipoles, in which the flat-sky analysis is expected to show some limitations anyway. A study like this, dealing with the impact of a component separation process on the CMB lensing reconstruction, has never been performed before. Our results allow us to assess that applying a component separation algorithm on the frequency channel CMB maps before any lensing estimation is a well-adapted strategy for the projected potential reconstruction within *Planck*.
2. For the full-sky reconstruction of the projected potential APS with *Planck*, we report that a realistic 11% of the sky mask, applied on some *Planck*-nominal lensed CMB temperature maps, has a negligible impact on the CMB lensing signal retrieval process, whenever it has been corrected by the *inpainting* method of Abrial et al. (2008) beforehand. More precisely, the bias on the estimated projected potential APS induced by the mask after inpainting is always either compatible with the theoretical 1σ errors (from $l = 300$ up to $l = 2600$) or weaker than the second-order in $C_l^{\phi\phi}$ non-Gaussian bias (in the $l < 300$ range). The major impact of the inpainting correction on the projected potential APS arises at the larger angular scales ($2 < l < 10$), which are not expected to be well-reconstructed with *Planck*. In addition, these results did not significantly change after the introduction of unresolved point source residuals. When treating the point sources emission in a comprehensive way, we report a 13% increase of the 1σ errors on the reconstructed deflection APS on average, resulting mainly from the unresolved point source residuals, whereas the level of bias is marginally increased at low multipoles. We conclude that applying the inpainting method of Abrial et al. (2008) beforehand is a good strategy to take into account the masking issue when seeking to reconstruct the projected potential with *Planck*.

Perspectives Our results on the CMB lensing reconstruction are the first step to develop a complete analysis chain dedicated to the projected potential APS reconstruction with the *Planck* data. This CMB lensing reconstruction pipeline should involve a component separation and a bright point sources detection followed by an algorithm to correct from the mask (e.g. the inpainting method) before applying a quadratic estimator of the projected potential field on the resulting CMB temperature map.

We plan to simultaneously work on both the flat-sky and the full-sky reconstruction tools. The flat-sky tools will allow us to perform a multi-patches CMB lensing reconstruction in cutting several hundred patches out of the most foreground-cleaned region of the full-sky map. Using such a method requires a quantitative study of the impact of the sphere-to-plan projection and the sharp edge cut effects beforehand. As a first task, we will test whether our results concerning the feasibility of reconstructing the CMB lensing after a component separation and after an inpainting of the mask still hold when dealing with the fully realistic *Planck* simulation (including e.g. a non-axisymmetric beam, inhomogeneous noise and correlated foreground emissions). As long as we can demonstrate we have sufficient control on the systematics, we will be ready to measure the projected potential

APS with *Planck* alone. This additional cosmological observable is expected to enlarge the investigation field accessible to the *Planck* mission from the primordial Universe to us.

Acknowledgements. We warmly thank Duncan Hanson for providing us the second-order non-Gaussian noise term biasing the projected potential APS estimation and for helpful discussions. We also thank Martin Reinecke for his help on the HEALPix package use. We acknowledge use of the CAMB, LENSPix, HEALPix-Cxx and MRS packages. This work was partially supported by the French National Agency for Research (ANR-05-BLAN-0289-01 and ANR-08-EMER-009-01).

References

Abrial, P., Moudden, Y., Starck, J., et al. 2007, J. Fourier Analysis and Applications, 13, 729
Abrial, P., Moudden, Y., Starck, J.-L., et al. 2008, Statistical Methodology, 5, 289
Aghanim, N., & Forni, O. 1999, A&A, 347, 409
Amblard, A., Vale, C., & White, M. 2004, New Astron., 9, 687
Argüeso, F., González-Nuevo, J., & Toffolatti, L. 2003, ApJ, 598, 86
Babich, D., & Pierpaoli, E. 2008, Phys. Rev. D, 77, 123011
Barreiro, R. B., Martínez-González, E., Vielva, P., & Hobson, M. P. 2006, MNRAS, 368, 226
Bernardeau, F. 1997, A&A, 324, 15
Blanchard, A., & Schneider, J. 1987, A&A, 184, 1
Bobin, J., Moudden, Y., Starck, J.-L., Fadili, J., & Aghanim, N. 2008, Statist. Methodol., 5, 307
Challinor, A., & Lewis, A. 2005, Phys. Rev. D, 71, 103010
Delabrouille, J., Melin, J.-B., & Bartlett, J. G. 2002, in AMiBA 2001: High-Z Clusters, Missing Baryons, and CMB Polarization, ASP Conf. Ser., 257, 81
Delabrouille, J., Cardoso, J.-F., & Patanchon, G. 2003, MNRAS, 346, 1089
Elad, M., & Starck, J.-L., Querre, P., & Donoho, D. 2005, Applied and Computational Harmonic Analysis, 19, 340
Górski, K. M., Hivon, E., Banday, A. J., et al. 2005, ApJ, 622, 759
Granato, G. L., De Zotti, G., Silva, L., Bressan, A., & Danese, L. 2004, ApJ, 600, 580
Guzik, J., Seljak, U., & Zaldarriaga, M. 2000, Phys. Rev. D, 62, 043517
Hanson, D., Challinor, A., Efstathiou, G., & Bielewicz, P. 2010, [arXiv:1008.4403]
Hirata, C. M., & Seljak, U. 2003a, Phys. Rev. D, 67, 043001
Hirata, C. M., & Seljak, U. 2003b, Phys. Rev. D, 68, 083002
Hirata, C. M., Ho, S., Padmanabhan, N., Seljak, U., & Bahcall, N. 2008, Phys. Rev. D, 78, 043520
Hu, W. 2000, Phys. Rev. D, 62, 043007
Hu, W. 2001a, Phys. Rev. D, 64, 083005
Hu, W. 2001b, ApJ, 557, L79
Hu, W. 2002, Phys. Rev. D, 65, 023003
Hu, W., & Okamoto, T. 2002, ApJ, 574, 566
Kamionkowski, M., Kosowsky, A., & Stebbins, A. 1997, Phys. Rev. Lett., 78, 2058
Kaplinghat, M., Knox, L., & Song, Y.-S. 2003, Phys. Rev. Lett., 91, 241301
Kesden, M., Cooray, A., & Kamionkowski, M. 2003, Phys. Rev. D, 67, 123507
Knox, L., & Song, Y.-S. 2002, Phys. Rev. Lett., 89, 011303
Komatsu, E. 2002, PhD thesis, Tohoku University
Leach, S. M., Cardoso, J., Baccigalupi, C., et al. 2008, A&A, 491, 597
Lesgourgues, J., Perotto, L., Pastor, S., & Piat, M. 2006, Phys. Rev. D, 73, 045021
Lewis, A. 2005, Phys. Rev. D, 71, 083008
Lewis, A., & Challinor, A. 2006, Phys. Rep., 429, 1
Lewis, A., Challinor, A., & Lasenby, A. 2000, ApJ, 538, 473
Masnou, S., & Morel, J.-M. 1998, in ICIP, ed. IEEE, 3, 259
Okamoto, T., & Hu, W. 2003, Phys. Rev. D, 67, 083002
Park, S. K., & Schowengerdt, R. A. 1983, Computer Graphics Image Processing, 23, 258
Perotto, L., Lesgourgues, J., Hannestad, S., Tu, H., & Y Y Wong, Y. 2006, J. Cosmology and Astro-Particle Physics, 10, 13
Riquelme, M. A., & Spergel, D. N. 2007, ApJ, 661, 672
Seljak, U., & Hirata, C. M. 2004, Phys. Rev. D, 69, 043005
Seljak, U. & Zaldarriaga, M. 1997, Phys. Rev. Lett., 78, 2054
Serjeant, S., & Harrison, D. 2005, MNRAS, 356, 192
Smith, K. M., Zahn, O., & Doré, O. 2007, Phys. Rev. D, 76, 043510
Su, M., & Yadav, A. P. S.and Zaldarriaga, M. 2009, Phys. Rev. D, 79, 123002
Sunyaev, R. A., & Zeldovich, Y. B. 1970, Comments on Astrophysics and Space Physics, 2, 66
Takada, M., & Futamase, T. 2001, ApJ, 546, 620
Tauber, J. A. 2006, in The Many Scales in the Universe: JENAM 2004 Astrophysics Reviews, ed. J. C. Del Toro Iniesta, E. J. Alfaro, J. G. Gorgas, E. Salvador-Sole, & H. Butcher, 35
The *Planck* Consortia 2005, Planck: the scientific programme, ESA-SCI(2006)1 (European Space Agency), [arXiv:astro-ph/0604069]
Zaldarriaga, M. 2000, Phys. Rev. D, 62, 063510
Zaldarriaga, M., & Seljak, U. 1998, Phys. Rev. D, 58, 023003